AIAA Journal
Vol. 61, No. 2, February 2023

Linear and Geometrically Nonlinear Structural Shape Sensing from Strain Data

Chan-Gi Pak*
NASA Neil A. Armstrong Flight Research Center, Edwards Air Force Base, California 93523-0273

https://doi.org/10.2514/1.J062165

An aircraft's shape must be measured during flight to implement active shape controls such as active trim shape, divergence, and sonic boom controls. A basis function method for linear as well as geometrically nonlinear structural shape sensing is proposed in this study. Basis functions can be mode shapes, linear static deformation shapes, and/or geometrically nonlinear static deformation shapes. The proposed basis function method is validated using a high-aspect-ratio wing, a swept test plate, and the National Aeronautics and Space Administration X-59 aircraft. A large structural deformation of a high-aspect-ratio wing is successfully captured using the proposed basis function method with less than 0.3% prediction error at the wing-tip section. The basis function method gives excellent deformation prediction, even with stress concentration. Performance of the basis functions is compared using the X-59 stabilator sample case. In most of the sample load cases, static deformations give a better correlation with the target deformation than do mode shapes. Wing shape sensing with sparse strain data are also demonstrated in this study using the X-59 aircraft. Predicted structural deformations match reasonably with the target deformations, even without strain gauges on some structural components. The predicted deformations have a good match with the target deformations.

Nomenclature

$h(\tilde{s})$	=	wing thickness at $\tilde{s}$, in
nn	=	number of nodes for an element
$\{q\}$	=	deformation vector
$\{q_i\}$	=	ith nodal deformation
$\{q_M\}$	=	master degrees of freedom
$\{q_S\}$	=	slave degrees of freedom
$\{q_s\}$	=	deformation vector at the sensor positions
$\{\tilde{q}_M\}$	=	measured master degrees of freedom
$\tilde{s}$	=	distance along the neutral axis direction, in.
$[\boldsymbol{T}]$	=	transformation matrix from strain to deformation
W_i	=	ith nodal weighting factor
$w(\tilde{s})$	=	deformation at $\tilde{s}$, in.
α	=	local angle due to wing taper or dihedral/anhedral effects
β	=	local sweep angle due to curvilinear sensor line effects
$\epsilon_l(\tilde{s})$	=	axial strain at $\tilde{s}$ on the lower skin
$\epsilon_u(\tilde{s})$	=	axial strain at $\tilde{s}$ on the upper skin
$\{\epsilon_i\}$	=	ith nodal strain
$\{\epsilon_s\}$	=	strain vector at the strain-gauge positions
$\{\tilde{\epsilon}_s\}$	=	measured strain vector at the strain-gauge positions
$\{\eta\}$	=	participation vector
$\theta(\tilde{s})$	=	slope at $\tilde{s}$, rad
$\kappa(\tilde{s})$	=	curvature at $\tilde{s}$; $\equiv -(\epsilon_u - \epsilon_l)/h$, in.$^{-1}$
$[\boldsymbol{\Phi}]$	=	deformation basis function matrix
$\boldsymbol{\Phi}_M$	=	deformation basis function matrix corresponding to master degrees of freedom
$\boldsymbol{\Phi}_S$	=	deformation basis function matrix corresponding to slave degrees of freedom
$[\boldsymbol{\Psi}_s]$	=	strain basis function matrix at the strain-gauge positions

Superscripts

T	=	transpose of a matrix
-1	=	inverse of a matrix

I. Introduction

The National Aeronautics and Space Administration (NASA) Helios aircraft experienced a total structural failure 30 min after takeoff from the island of Kauai, Hawaii, on 26 June 2003. Before the mishap, the aircraft faced turbulence and started a divergent pendulum motion in the pitch direction caused by a high-center-of-gravity location and the "persistent" high dihedral configuration [1]. An aeroelastic stability analysis of the aircraft was performed during the mishap investigation. This analysis showed that one of the flexible modes of the aircraft became highly damped at zero frequency (that is, an overdamped response to external loads) before the mishap (page 41 of Ref. [1]). The following two recommendations were prepared in the mishap investigation report (page 93 of Ref. [1]).
Recommendation 1: Develop a method to measure wing dihedral in real time with a visual display available to the test crew.
Recommendation 2: Develop manual and/or automatic techniques to control wing dihedral in flight.

Geometrically large trim shape sensing for an aircraft during flight is important for a highly flexible aircraft with a high-aspect-ratio wing, such as a high-altitude long-endurance aircraft, a transonic truss-braced wing aircraft (The Boeing Company, Chicago, Illinois), and the NASA Ikhana aircraft. The time history of the terminal event of the NASA Helios aircraft (247 ft wingspan) shows a steady increase in dihedral up to 40 ft (page 37 of Ref. [1]) (see Fig. 1), meaning that a large deflection of the wing tip of nearly 32% of the wing semispan occurred before the mishap. Linear wing shape-sensing techniques cannot properly predict such a large structural deformation.

An objective of the jig-shape optimization study for the NASA X-59 Quiet Supersonic Technology (known as QueSST) aircraft [2], shown in Fig. 2,[†] is to minimize the error between the aeroelastic trim shape and the target trim shape at cruise flight speed. The computation of the target trim shape was based on rigid aircraft assumptions. The updated jig shape is optimum only at the design cruise flight condition, which is

Presented as Paper 2023-2418 at the AIAA Scitech 2023 Forum, National Harbor, MD, January 23–27, 2023; received 16 June 2022; revision received 26 September 2022; accepted for publication 19 October 2022; published online 28 November 2022.

*Subject Matter Expert in Analytical Structural Dynamics, Aerostructures Branch, P.O. Box 273, Mailstop 48202A.

[†]Images available online at https://www.nasa.gov/mission_pages/lowboom/images [retrieved 1 September 2022].

a) During takeoff

b) Before the mishap

Fig. 1 Helios aircraft a) during takeoff and b) before the mishap [1].

Fig. 2 X-59 Quiet Supersonic Technology aircraft. Credit: Lockheed Martin.

the primary limitation of this jig-shape optimization study. When the flight condition and the aircraft weight configuration are changed during flight, the updated jig shape is "not optimum." The strength of a sonic boom on the ground can be reduced with active trim shape control.

Historically, structural deformation is not easy to measure during flight; however, structural deformation must be measured during flight in order to implement an active shape control technique, such as active dihedral control, active divergence suppression, active buckling suppression, maneuver load alleviation, gust load alleviation, or active sonic boom control. A linear shape sensing of a flat plate using the measured strain data together with the least-squares surface fitting technique has been introduced by Foss and Haugse [3]. In this approach, the deformation and corresponding strain "mode shapes" were used for the computation of the transformation matrix between the strain input and the deformation output. Applications of this approach using strain data measured from fiber-optic strain sensing (FOSS) were observed in Refs. [4,5]. Deformation computation of the aircraft structures using an inverse finite element (FE) method has been introduced by Tessler and Spangler [6]. First, a "simplified" three-dimensional (3-D) structural FE model is created in this inverse FE method. Then, errors between measured and computed strain data are minimized using a model tuning technique. Deformations at distributed sensor positions are available from the tuned FE model.

For real-time linear shape sensing, closed-form equations for the computation of structural deformation from the measured strain data have been derived by Ko et al. [7]. Wing deflection along a line is available during wind-tunnel testing using a FOSS system [5]. Full-field deformation, however, is not available; and deformation values are only available along the line of the FOSS installation [8,9]. The two-step theory for real-time linear shape sensing of a full 3-D structure has been introduced by Pak [10]. The first step is the computation of structural deformation along the neutral axis using a numerical integration of curvature based on the linear least-squares method and cubic spline techniques. Curvature along the neutral axis is obtained using strain data and wing thickness information. This curvature is integrated twice to compute deformation along the neutral axis. The second step is to extrapolate deformation along the neutral axis to the entire aircraft structure to obtain distributed deflection as well as slope information. To date, this linear two-step theory has been demonstrated using simple platelike structures [10–12] as well as wings with spars and ribs [13]. Nonlinear shape-sensing techniques have also been introduced [14–16]. The NASA Neil A. Armstrong Flight Research Center used deformation sensing to suppress the flutter in the X-56A aircraft [17]. In this active flutter suppression study, the computer-simulated strain data are used for the shape-sensing procedure.

The primary objective of the current study is to introduce a basis function method for predicting linear as well as geometrically nonlinear structural deformation using strain data. Mode shapes, linear static deformation shapes, and geometrically nonlinear static deformation shapes can be used as basis functions in this approach. The proposed method is validated using four example cases.

II. Mathematical Background of Basis Function Method

The approach by Foss and Haugse [3] requires an analytical model. On the other hand, Ko et al.'s closed-form solution [7] as well as the first step of the two-step theory by Pak [10] do not need an analytical model. The latter approaches, however, require the deformation and slope boundary conditions at the starting point of the integration procedure. For most of the cantilevered test articles, it is assumed that the deformation and slope at the wing root section are equal to zero; however, when strain measurement starts in an intermediate position such as the junction between the wing and fuselage, then it is difficult to use zero deformation and slope assumptions. Moreover, errors in boundary conditions will propagate into the rest of the integrations. An analytical model is also needed in the current proposed method; however, it does not require any boundary conditions.

A. Basis Function Method

The basis function method in this study is similar to the least-squares surface fitting technique by Foss and Haugse [3]. Assume that the deformation vector $\{q\}$ in Eq. (1) and the strain vector $\{\epsilon_s\}$ at the strain-gauge positions in Eq. (2) are defined using the same participation vector $\{\eta\}$ as follows:

$$\{q\} = [\mathbf{\Phi}]\{\eta\} \tag{1}$$

$$\{\epsilon_s\} = [\mathbf{\Psi}_s]\{\eta\} \tag{2}$$

where columns of the matrix $[\mathbf{\Phi}]$ are the shapes of deformation basis functions. Similarly, the columns of the matrix $[\mathbf{\Psi}_s]$ are the shapes of strain basis functions. Each column of the matrix $[\mathbf{\Phi}]$ corresponds to each column of the matrix $[\mathbf{\Psi}_s]$. The deformation vector $\{q\}$ and the matrix $[\mathbf{\Phi}]$ are defined in the global coordinate. On the other hand, strain vector $\{\epsilon_s\}$ and the corresponding matrix $[\mathbf{\Psi}_s]$ have their own strain-gauge coordinates at each strain-gauge location based on the uniaxial strain-gauge direction. For example, one rosette is defined at a strain-gauge location, then this rosette is separated to three uniaxial strain-gauges with three strain-gauge coordinates at the same location. Therefore, the strain values computed using the MSC Nastran code in the element coordinates should be transformed to the strain-gauge coordinates.

The participation vector $\{\eta\}$ is obtained using the least-squares surface fitting technique. Multiplying the matrix $[\boldsymbol{\Psi}_s]^{\mathrm{T}}$ to Eq. (2) gives Eq. (3) and finally the vector $\{\eta\}$ becomes Eq. (4).

$$[\boldsymbol{\Psi}_s]^{\mathrm{T}}\{\epsilon_s\} = [\boldsymbol{\Psi}_s]^{\mathrm{T}}[\boldsymbol{\Psi}_s]\{\eta\} \tag{3}$$

$$\{\eta\} = ([\boldsymbol{\Psi}_s]^{\mathrm{T}}[\boldsymbol{\Psi}_s])^{-1}[\boldsymbol{\Psi}_s]^{\mathrm{T}}\{\epsilon_s\} \tag{4}$$

Substituting Eq. (4) into Eq. (1) gives Eq. (5).

$$\{q\} = [\boldsymbol{\Phi}]([\boldsymbol{\Psi}_s]^{\mathrm{T}}[\boldsymbol{\Psi}_s])^{-1}[\boldsymbol{\Psi}_s]^{\mathrm{T}}\{\epsilon_s\} = [\boldsymbol{T}]\{\epsilon_s\} \tag{5}$$

Therefore, the transformation matrix $[\boldsymbol{T}]$ from the strain input $\{\epsilon_s\}$ to the deformation output $\{q\}$ becomes as shown in Eq. (6).

$$[\boldsymbol{T}] = [\boldsymbol{\Phi}]([\boldsymbol{\Psi}_s]^{\mathrm{T}}[\boldsymbol{\Psi}_s])^{-1}[\boldsymbol{\Psi}_s]^{\mathrm{T}} \tag{6}$$

The numbers of rows for matrices $[\boldsymbol{\Phi}]$ and $[\boldsymbol{\Psi}_s]$ are the total number of deformation degrees of freedom (DOF) to be measured and the total number of uniaxial strain and shear measurements, respectively. The column number of matrices $[\boldsymbol{\Phi}]$ and $[\boldsymbol{\Psi}_s]$ is equal to the number of basis functions used in this transformation. Substituting Eq. (4) into Eq. (2) gives Eq. (7):

$$\{\epsilon_s\} = [\boldsymbol{\Psi}_s]([\boldsymbol{\Psi}_s]^{\mathrm{T}}[\boldsymbol{\Psi}_s])^{-1}[\boldsymbol{\Psi}_s]^{\mathrm{T}}\{\tilde{\epsilon}_s\} \tag{7}$$

where $\{\tilde{\epsilon}_s\}$ and $\{\epsilon_s\}$ are the measured and fitted strain vectors at the strain-gauge locations, respectively. The performance of this surface fitting depends on the number of the basis functions and how close the basis function shapes are to the target shape.

Candidate basis function shapes in the matrix $[\boldsymbol{\Phi}]$ can be

1) deformation mode shapes,

2) linear static deformation shapes under a variety of load conditions, or

3) geometrically nonlinear static deformation shapes under a variety of load conditions.

Therefore, the corresponding strain shapes at the strain-gauge positions in the matrix $[\boldsymbol{\Psi}_s]$ are obtained. When only the mode shapes are selected as the basis function shapes, then the proposed basis function method becomes the method developed by Foss and Haugse [3]. In this study, static deformation shapes are also selected as the basis functions.

A basic guideline for selecting the static deformation shapes is to use similar flight load conditions to that of the target flight load. The transformation matrix in Eq. (6) is based on a least-squares surface fitting procedure, which is basically a minimization of the error between target (measured) strain and simulated target strain. If the basis strain shapes are like the target strain shape, then the performance of the surface fitting will be improved.

B. Computation of Strain at the Strain-Gauge Positions

In the case of the MSC Nastran code [18], the structural deformation and strain values can be computed at the nodal points. It is assumed that the deformation sensing and strain-gauge center positions are located inside each FE. Deformation and strain values at any random position inside each FE are computed using the nodal deformation $\{q_i\}$ and nodal strain $\{\epsilon_i\}$ values together with the nodal weighting factors W_i, which can be obtained using isoparametric shape functions [19]. The deformation and strain vectors, $\{q_s\}$ and $\{\epsilon_s\}$, at the deformation sensors and strain gauges are computed using Eqs. (8) and (9):

$$\{q_s\} = \sum_{i=1}^{nn} W_i\{q_i\} \tag{8}$$

$$\{\epsilon_s\} = \sum_{i=1}^{nn} W_i\{\epsilon_i\} \tag{9}$$

where nn is four in the case of the quadrilateral plate element with four nodes, the six-sided solid element with eight nodes, and the five-sided solid element with six nodes (CPENTA; quadrilateral faces) [18]. Similarly, nn is three for the triangular plate element with three nodes, the CPENTA (triangular faces), and the four-sided solid element with four nodes; and it is two for the simple bar element with two nodes and the beam element with two nodes [18]. The computation of the nodal weighting factors W_i for a deformation or strain at any sensor position inside an FE is explained in Appendix A.

III. Numerical Validation of the Basis Function Method and Discussion

The proposed basis function method is validated in this section using four example cases. These four cases (a high-aspect-ratio wing, a swept test plate, the stabilator of the X-59 QueSST aircraft, and the X-59 QueSST aircraft itself) are discussed in the following:

A. High-Aspect-Ratio Wing

In this study, the wing shape prediction of a high-aspect-ratio wing with a large dihedral angle is performed. The FE model of this rectangular wing (as well as its span and chord lengths, wing and plate thicknesses, and material properties) is shown in Fig. 3. The

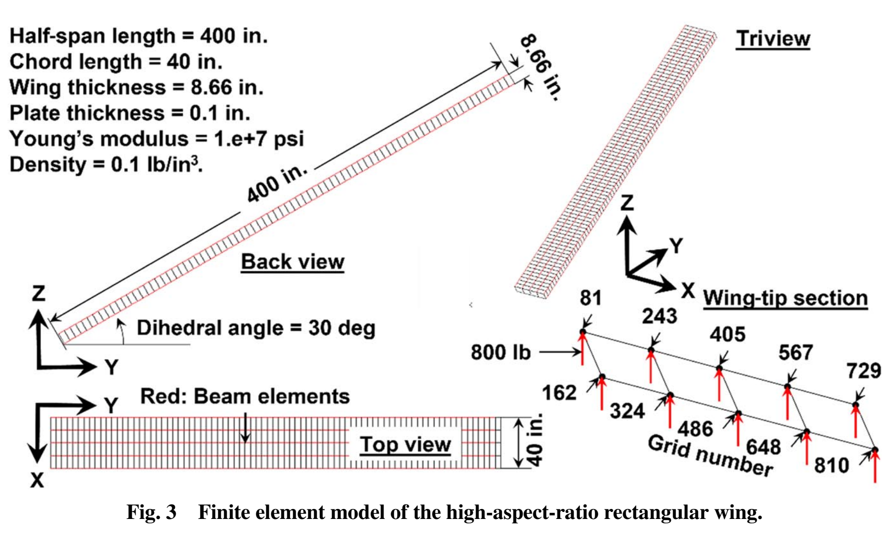

Fig. 3 Finite element model of the high-aspect-ratio rectangular wing.

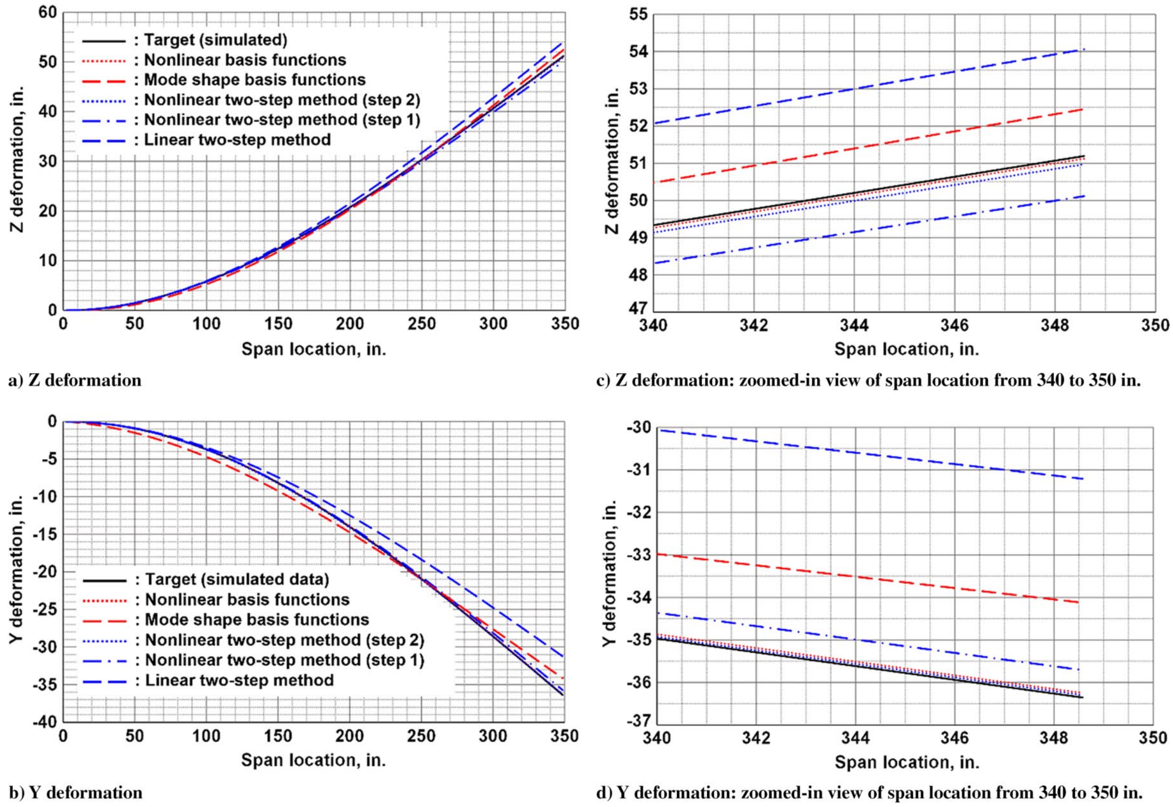

a) Z deformation

b) Y deformation

c) Z deformation: zoomed-in view of span location from 340 to 350 in.

d) Y deformation: zoomed-in view of span location from 340 to 350 in.

Fig. 4 Comparisons of structural shape-sensing techniques using a rectangular wing model.

wing-tip section plot with candidate applied loads is also illustrated in Fig. 3. The y and z deformations based on the basis function method, with mode shapes [3] and static deformation shapes from geometrically nonlinear static analysis as the basis functions, are compared with results obtained using the linear [10] as well as nonlinear two-step theories, as shown in Fig. 4. The nonlinear two-step theory is explained in Appendix B.

First, 10 flexible mode shapes are selected for the linear basis function method and the linear two-step theory. On the other hand, 31 nonlinear static deformation shapes under 31 different static load cases (given in Table 1) are used for the nonlinear basis function method. A total of 810 simulated uniaxial strain data values from the upper and lower skins are used in this sample test.

In general, results from the basis function method have a better correlation with the simulated target deformations than do the results from the two-step theory. The simulated target deformation under the target load in Table 1 is generated using the MSC Nastran code. Target deformations are compared with predicted deformations at the wing-tip location, as shown in Table 2. The prediction difference using the nonlinear basis functions is less than 0.3% at the wing-tip section. The nonlinear two-step theory (Table 2) gives the second-best correlation with the target deformations, where prediction differences are less than 2.2% after the first step and less than 0.5% after the second step. The nonlinear two-step theory after the second step gives the same quality of results as the nonlinear basis function method.

In the case of using mode shapes, the basis function method gives better results than does the two-step theory. It should be noted that large prediction differences of 6.13 and 14.1% are observed (Table 2). These differences are mainly due to the linear assumption of the large deformation.

B. Swept Test Plate

The next sample problem is based on the swept test plate shown in Fig. 5, which was fabricated and tested at the NASA Neil A. Armstrong Flight Research Center [8]. This cantilevered test plate has a 45 deg swept angle with a uniform chord and half-span lengths of 12 and 35.36 in., respectively. Material properties and the FE model of the test plate were given in Ref. [10]. Twelve loading points with spanwise locations are given in Fig. 5. The FOSS layout for the strain data collection is also provided in Fig. 5.

Sixteen nonlinear static deformations as well as 10 mode shapes are selected as basis functions in this example. Static deformations are obtained using 16 different load cases, shown in Fig. 6. Loading points are also shown in Fig. 6. The deformations and strains in Eq. (6) for the basis function method are computed using the MSC Nastran code. On the other hand, strains $\{\epsilon_s\}$ in Eq. (5) and target deformations that correspond to load cases 1, 2, and 4 are measured during the test [8]. In this study, load cases 1, 2, and 4 are called the leading-edge load, the uniform load, and the point load, respectively.

The measured plate tip deformations are given in Table 3. Three different approaches to shape-sensing techniques are compared in this table. These three approaches are the Ko displacement theory [7,8], the two-step theory [10], and the basis function method. The maximum relative errors from these three approaches are 4.4, 3.8, and 2.3% in the leading-edge load case. On the other hand, 3.8, 2.6, and 0.53% are observed in the uniform load case. Finally, the Ko displacement theory is compared with the basis function method in the point load case. The maximum errors are 5.05 and 1.21%.

It should be noted that the Ko displacement theory and the two-step theory are based on the linear assumption. The basis function method in this example, however, uses nonlinear static deformations as well as mode shapes to capture linear and nonlinear deformations properly. The fiber lengths along the leading edge, midchord, and trailing edge are 50 in. Therefore, the maximum deformations divided by the fiber lengths for the three load cases are 10.6, 15.9, and 18.1%, respectively.

Strain and deformation values under the point load case (case 4 in Fig. 6) are shown in Fig. 7. Predicted deformations using the basis function method are compared with the measured target

Table 1 Applied loads for high-aspect-ratio rectangular wing box[a]

	Grid number (800 lb upward, $+Z$ direction, load at each grid)									
Load case for basis functions	81	162	243	324	405	486	567	648	729	810
1	I	I	——	——	——	——	——	——	——	——
2	——	——	I	I	——	——	——	——	——	——
3	——	——	——	——	I	I	——	——	——	——
4	——	——	——	——	——	——	I	I	——	——
5	——	——	——	——	——	——	——	——	I	I
6	I	I	I	I	——	——	——	——	——	——
7	I	I	——	——	I	I	——	——	——	——
8	I	I	——	——	——	——	I	I	——	——
9	I	I	——	——	——	——	——	——	I	I
10	——	——	I	I	I	I	——	——	——	——
11	——	——	I	I	——	——	I	I	——	——
12	——	——	I	I	——	——			I	I
13	——	——	——	——	I	I	I	I		
14	——	——	——	——	I	I	——	——	I	I
15	——	——	——	——	——	——	I	I	I	I
16	I	I	I	I	I	I	——	——	——	——
17	I	I	I	I	——	——	I	I	——	——
18	I	I	I	I	——	——	——	——	I	I
19	I	I	——	——	I	I	I	I	——	——
20	I	I	——	——	I	I	——	——	I	I
21	I	I	——	——	——	——	I	I	I	I
22	——	——	I	I	I	I	I	I	——	——
23	——	——	I	I	I	I	——	——	I	I
24	——	——	I	I	——	——	I	I	I	I
25	——	——	——	——	I	I	I	I	I	I
26	I	I	I	I	I	I	I	I	——	——
27	I	I	I	I	I	I	——	——	I	I
28	I	I	I	I	——	——	I	I	I	I
29	I	I	——	——	I	I	I	I	I	I
30	——	——	I	I	I	I	I	I	I	I
31					9 G load					
Load for generation of target deformation	I	I	I	I	I	I	I	I	I	I

[a]I denotes "included."

Table 2 Wing-tip deformation of high-aspect-ratio rectangular wing box

		Basis function method				Two-step theory					
		Nonlinear		Linear		Nonlinear (after step 2)		Nonlinear (after step1)		Linear	
Deformation	Target	Value	Difference	Value	Difference	Value	Difference	Value	Difference	Value	Difference
Y, in.	−36.35	−36.25	−0.29%	−34.12	−6.13%	−36.30	−0.15%	−35.71	−1.77%	−31.21	−14.1%
Z, in.	51.19	51.12	−0.14%	52.45	2.46%	50.97	−0.43%	50.12	−2.11%	54.06	5.60%

deformations in Fig. 7c. Because of the large sweep angle in this swept test plate case, a stress concentration exists near the trailing edge of the plate root section, as shown in Fig. 7a. High measured strain values are found from 1 to 4 in. of the trailing-edge fiber locations, as shown by the green and blue circles in Fig. 7b.

The Ko displacement theory [7,8] and the first step of the two-step theory [10] are based on the integration of the curvature along the FOSS line. The integration of curvatures along the trailing-edge fiber line is independent of curvatures along the other two fiber lines. The accuracy of the predicted deformation depends on the existence of the stress concentration near the FOSS line. As shown in Fig. 7b, these high strain values with large slopes should be extrapolated to have the strain value at the centerline where integration begins in the Ko displacement theory and the first step of the two-step theory. Therefore, extrapolation errors in the computation of deformation at the plate root section are propagated to the plate tip section. All three load cases exhibit the stress concentration phenomenon. Therefore, relative errors at the trailing edge of the plate tip are larger than the other two (leading edge and middle) in the case of the Ko displacement theory and the first step of the two-step theory.

The second step of the two-step theory is based on least-squares surface fitting. Therefore, errors from the first step of the two-step theory are smoothed as shown in Table 3. The errors of 3.90, 2.80, and 0.79 become smaller errors (3.80, 2.60, and 0.25, respectively); and errors of 0.65, 0.38, and 1.40 become larger errors (1.40, 0.97, and 2.20, respectively). Therefore, the relative errors along one fiber are affected by the relative errors of the other two fibers with the least-squares surface fitting.

In general, the linear Ko displacement theory and the two-step method create a larger prediction error than the basis function method, as shown in Table 3. The basis function method is based on the least-squares surface fitting technique of the measured strain. The quality of the predicted deformations is not affected by the local stress concentration, as shown by the maximum relative errors of 2.25, 0.53, and 1.21 percent. In the leading-edge and uniform load cases, the maximum relative errors are at the trailing-edge tip position. On the other hand, the maximum relative error is at the

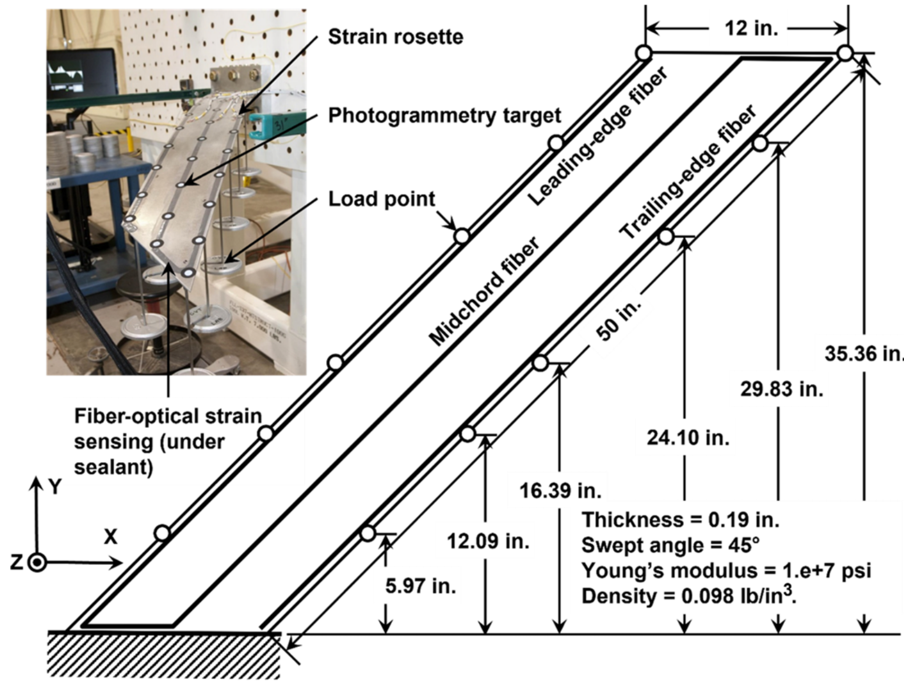

Fig. 5 Swept test plate [10].

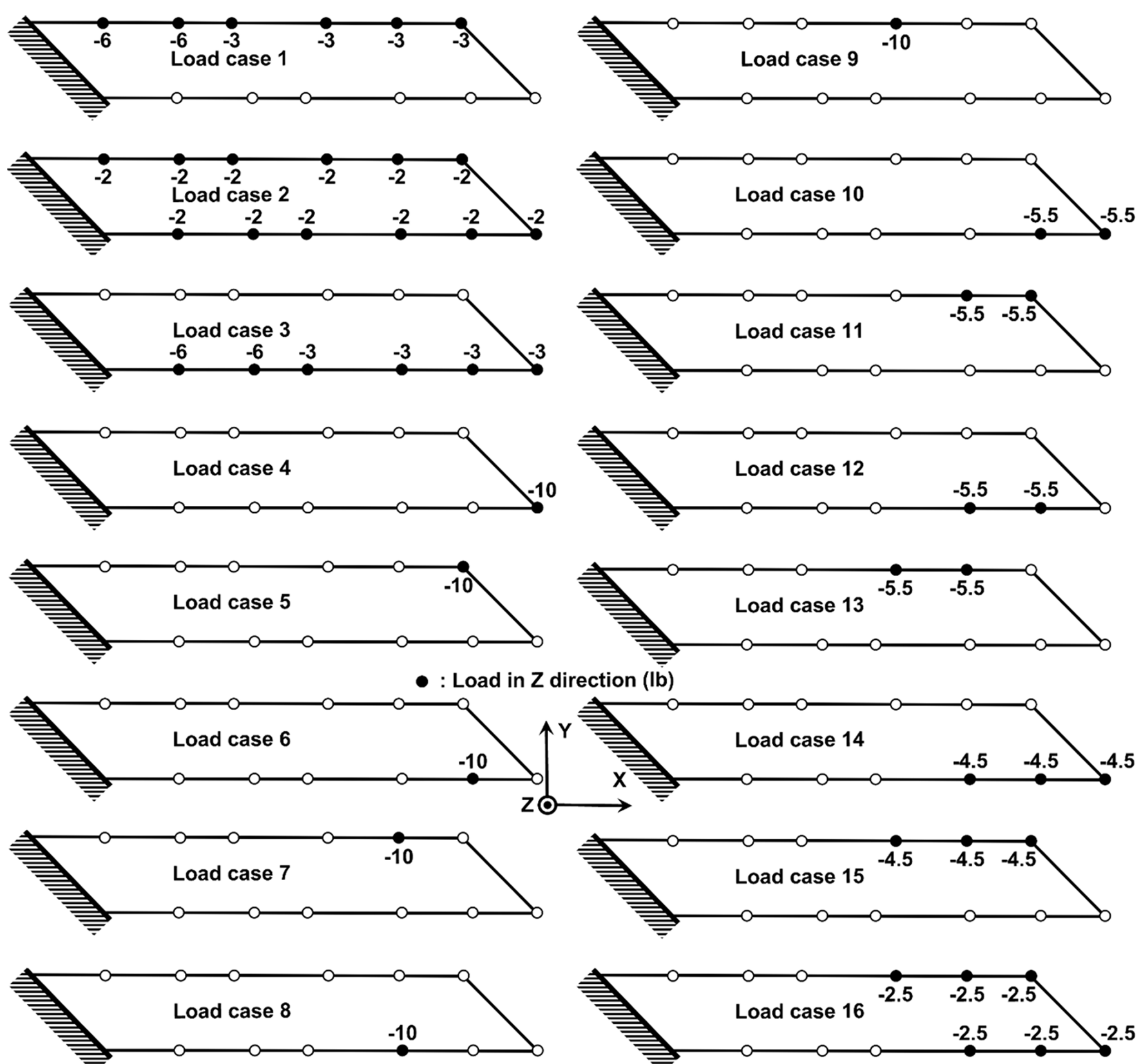

Fig. 6 Sixteen load cases for generating basis functions.

Table 3 Swept test plate deformation at plate tip[a]

Fiber location	Measured, in.	Computed, in.			Relative error, %		
		Bakalyar and Jutte [8]	Two-step method [10]	Basis function	Bakalyar and Jutte [8]	Two-step method [10]	Basis function
Leading–edge load (load case 1)							
Leading edge	−4.525	−4.500	−4.569(−4.542)[b]	−4.493	−0.55	0.97(0.38)	−0.72
Middle	−4.912	−4.952	−4.843(−4.880)	−4.835	0.81	−1.40(−0.65)	−1.57
Trailing edge	−5.300	−5.067	−5.097(−5.091)	−5.180	−4.40	−3.80(−3.90)	−2.25
Uniform load (load case 2)							
Leading edge	−6.541	−6.546	−6.684(−6.630)	−6.549	0.08	2.20(1.40)	0.12
Middle	−7.256	−7.408	−7.238(−7.313)	−7.234	2.10	−0.25(0.79)	−0.30
Trailing edge	−7.971	−7.667	−7.763(−7.750)	−7.929	−3.80	−2.60(−2.80)	−0.53
Point load at trailing edge of plate tip (load case 4)							
Leading edge	−7.087	−7.007	N/A	−7.172	−1.13	N/A	1.21
Middle	−8.073	−8.145	N/A	−8.140	0.89	N/A	0.83
Trailing edge	−9.058	−8.601	N/A	−9.137	−5.05	N/A	0.87

[a]N/A = Not Available.
[b]After step 1 computation.

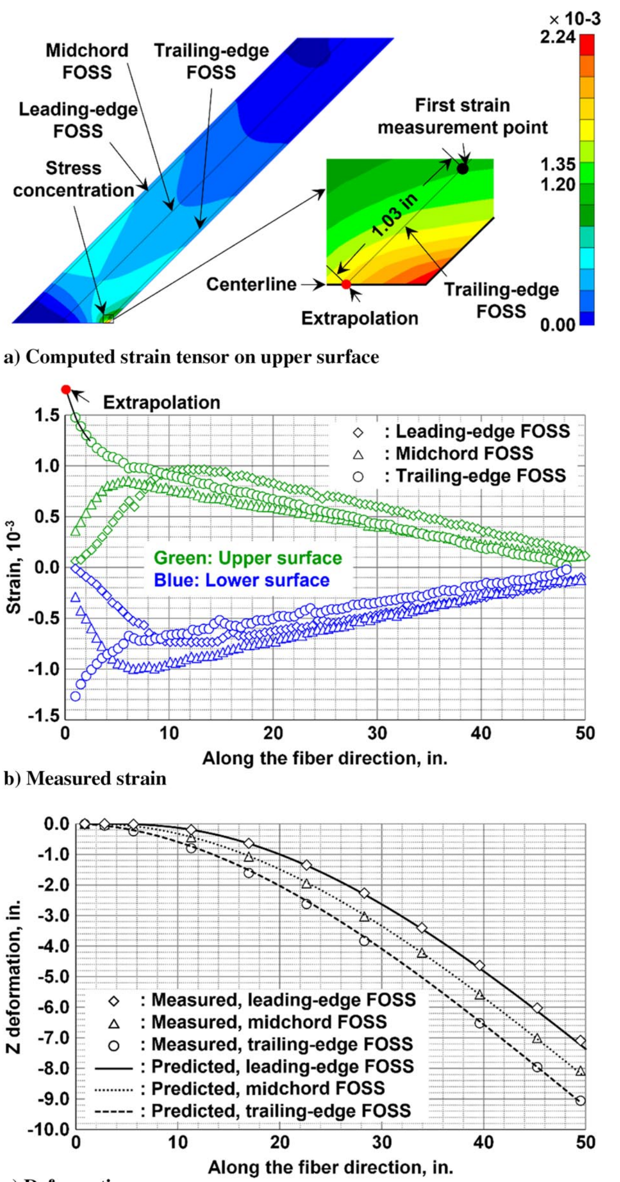

Fig. 7 Strain and deformation of the swept test plate under a point load case.

leading-edge tip position in the point load case, although the stress concentration exists near the trailing-edge FOSS of the plate root section.

C. X-59 Stabilator

The structural shape prediction for the stabilator of the X-59 QueSST aircraft during pretest analysis is presented in this subsection. All the mode shapes, static deformations, and strain data used in this subsection are computed using the MSC Nastran code. The FE models of the stabilator as well as the positions of the strain-gauge rosettes and the string potentiometers are shown in Fig. 8. In this example, 30 computer simulated uniaxial strain values are used: one for each side of the stabilator.

The first 20 flexible mode shapes (10 for each side of the stabilator) together with seven linear static deformation shapes corresponding to load cases 1 through 7 under different flight conditions (shown in Fig. 9) are used as the basis functions in this sample test. These deformation shapes for the basis function are also used for the target deformation shapes in this subsection. These seven load cases were used during the proof and calibration tests for the stabilators of the X-59 QueSST aircraft. In this subsection, three different groups of the basis functions are used for the prediction of the target deformation shapes. Mode shapes and the linear static deformation shapes under different load cases belong to the first and second groups, respectively. The combination of the first and second groups becomes the third group.

Graphical visualizations of the target as well as predicted deformation shapes based on the three different basis function groups are shown in Fig. 10. Comparisons of the target and predicted deformations are also given in Table 4. The maximum target deformations for each load case in the second column of Table 4 are also provided in Fig. 10 with black arrows. The maximum prediction differences based on different basis function groups are also provided in Table 4. In general, the group 3 basis functions give the smallest percentage difference at the maximum target deformation position, except for load case 1. The maximum differences using the group 3 and group 2 basis functions (−0.044 and −0.047 in., respectively) are smaller than the 0.065 in obtained using the group 1 basis functions. When using the group 1 basis functions, the maximum difference between the target and predicted deformations occurs at string potentiometer identification (ID) number 20, which is indicated by the blue arrow in Fig. 10a. In this case, the maximum prediction difference is a more meaningful measure of accuracy than comparing the percentage differences.

The participation factors for each load case are summarized in Table 5. In this table, basis functions 1 through 7 are obtained from

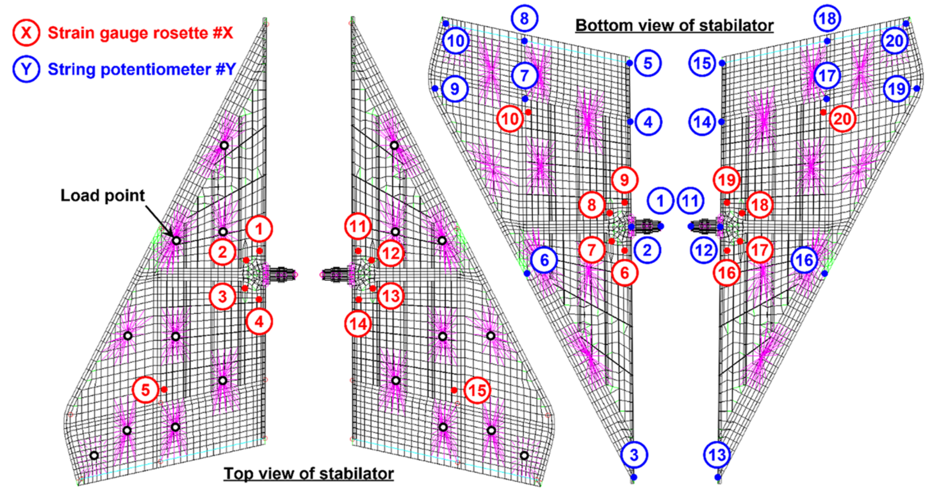

Fig. 8 **Positions of strain-gauge rosettes and string potentiometers for the X-59 stabilator.**

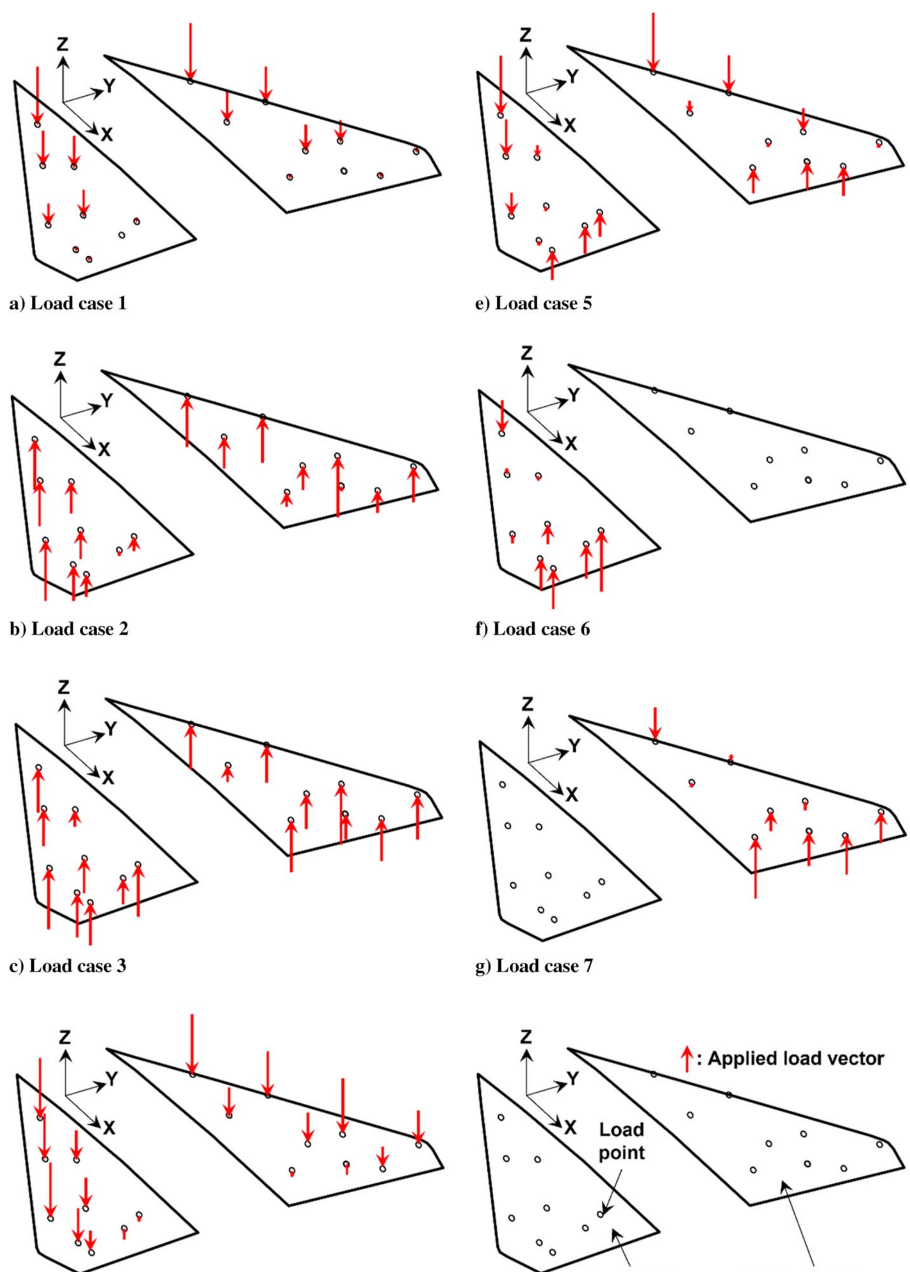

a) Load case 1

b) Load case 2

c) Load case 3

d) Load case 4

e) Load case 5

f) Load case 6

g) Load case 7

Fig. 9 **Seven load cases for the generation of the target and basis function shapes.**

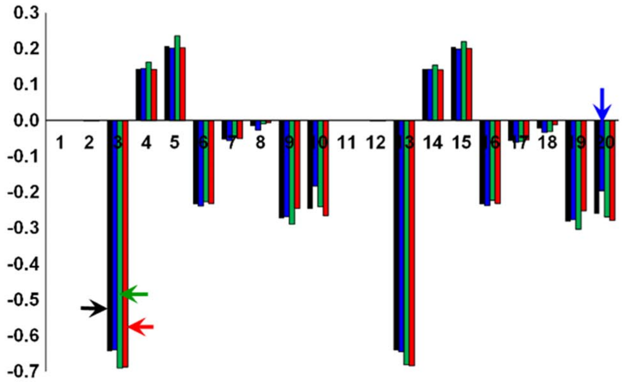

a) Load case 1

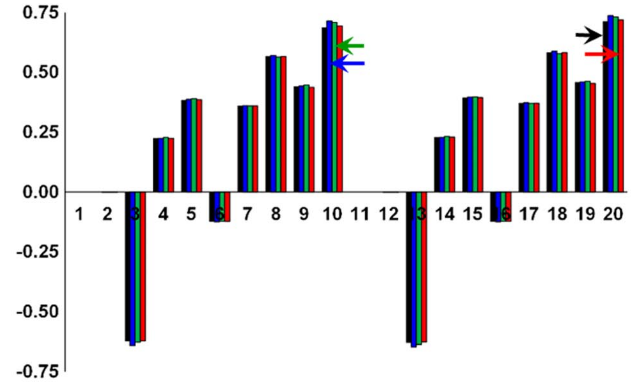

e) Load case 5

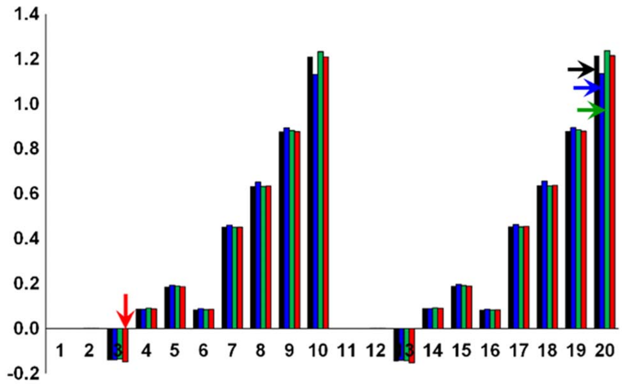

b) Load case 2

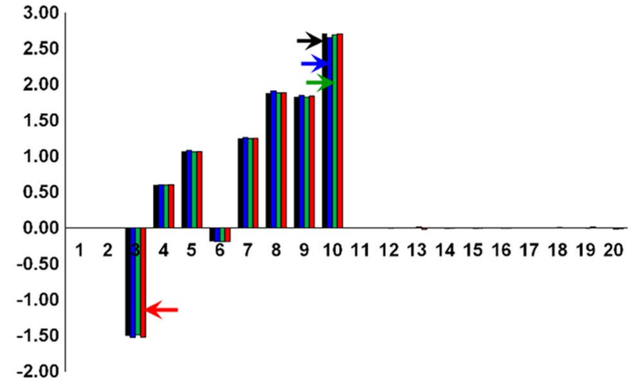

f) Load case 6

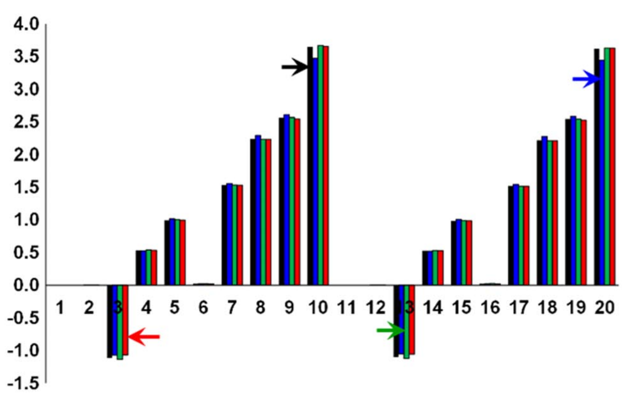

c) Load case 3

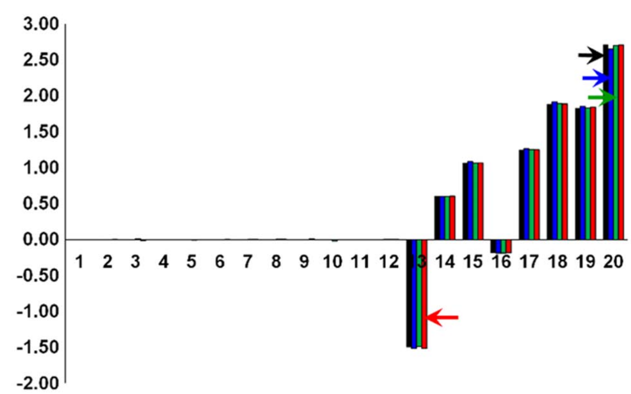

g) Load case 7

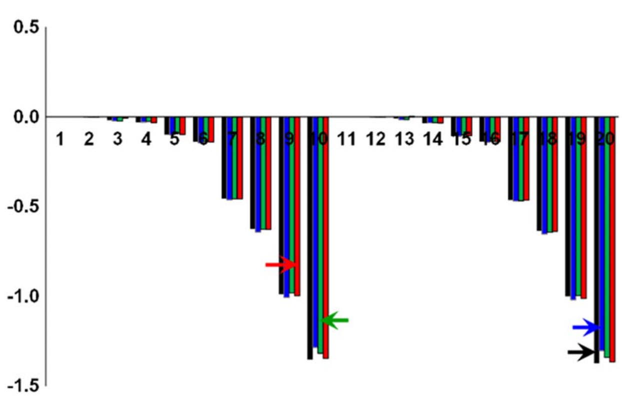

d) Load case 4

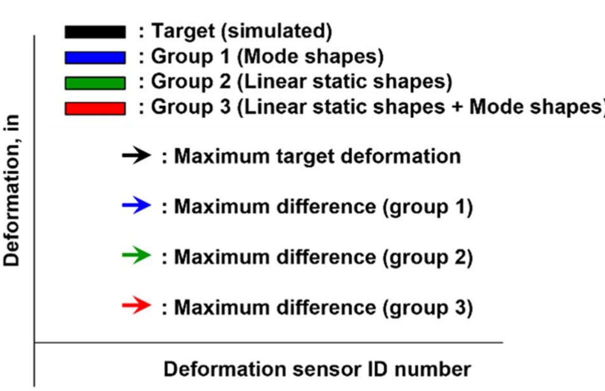

Fig. 10 Comparisons of vertical deformations under different basis function groups for seven load cases.

Table 4 Comparisons of Z deformation using different basis functions[a]

Load case	Maximum target deformation, in. (pot. ID #)	Group 1 (mode shapes: 20) Difference, in. (%)[b]	Group 1 Maximum difference, in. (pot. ID #)[c]	Group 2 (static shapes: 6) Difference, in. (%)	Group 2 Maximum difference, in. (pot. ID #)[c]	Group 3 (static + mode shapes: 26) Difference, in. (%)[c]	Group 3 Maximum difference, in. (pot. ID #)[c]
1	−0.643(3)	0.004(−0.6)	0.065(20)	−0.047(7.3)	−0.047(3)	−0.044(6.8)	−0.044(3)
2	1.213(20)	−0.078(−6.5)	−0.078(20)	0.022(1.8)	0.022(20)	0.001(0.1)	−0.008(3)
3	3.647(10)	−0.172(−4.7)	−0.174(20)	0.020(0.5)	−0.021(13)	0.010(0.3)	0.046(3)
4	−1.372(20)	0.070(−5.1)	0.070(20)	0.031(−2.3)	0.035(10)	0.006(−0.4)	−0.010(9)
5	0.713(20)	0.024(3.4)	0.026(10)	0.018(2.5)	0.021(10)	0.006(0.8)	0.006(20)
6	2.712(10)	−0.060(−2.2)	−0.060(10)	−0.020(−0.7)	−0.020(10)	−0.007(−0.3)	−0.017(3)
7	2.712(20)	−0.060(−2.2)	−0.060(20)	−0.016(−0.6)	−0.016(20)	−0.007(−0.3)	−0.017(13)

[a]Pot. ID # denotes the string potentiometer identification number
[b]Difference at the maximum target deformation
[c]Maximum difference of the measured deformation

the linear static deformation analysis using load cases 1 through 7 in Fig. 9. On the other hand, basis functions 8 through 17 are the first 10 mode shapes of the stabilator, with five modes for each side. Mode numbers 1, 2, 4, and 5 on each side of the stabilator are mainly used to fit the target shape when the group 1 basis functions are used. The number of basis functions for group 2, which is six, is smaller than the group 1 case, which is 20, even with better prediction performance. It should be noted that the high-frequency mode shapes (basis function 18 through 27) do not contribute much to the surface fitting procedures with the group 1 and group 3 cases, mainly due to the surface wiggling of the high-frequency mode shapes. The ith basis function, which includes basis functions 1 through 7, should not be used for the prediction of the ith target deformation because these two have the same shape. When the i basis function is used for fitting the ith target deformation, then the ith participation factor becomes 1.0 and all the other participation factors will be zero.

D. X-59 QueSST Aircraft

The proof test configuration of the X-59 QueSST aircraft is shown in Fig. 11.[‡] The FE model and the locations of the strain gauges as well as string potentiometers are shown in Fig. 12. In this test, string potentiometers are distributed symmetrically, as shown in Fig. 12 with blue circles. On the other hand, most strain gauges (red circles in Fig. 12) are located on the left-hand side of the aircraft. The right-hand-side strain gauges are mainly located near the main landing gear bay area. There are no strain gauges on the right wing, canards, t tails, flaps, or ailerons.

The first 30 flexible mode shapes and linear static deformation shapes under 25 different flight load cases are selected as the basis functions in this example. The deformation and strain basis function shapes used for the computation of the transformation matrix [T] in Eq. (6) are computed using the MSC Nastran code. Three groups of the basis function are also used in this section: 1) group 1 (30 mode shapes), 2) group 2 (25 linear static deformation shapes), and 3) group 3 (group 1 basis functions and group 2 basis functions). The total numbers of uniaxial strain measurements and string potentiometers in Fig. 12 are 321 and 41, respectively.

When the predicted deformations using the basis function method are compared with the simulated target deformations using load case 2, the basis functions are static deformation shapes under load cases 1 and 3 through 25, as well as 30 mode shapes, as shown in Fig. 13. In this computation, the strain values $\{\epsilon_s\}$ in Eq. (5) are computed using the MSC Nastran code. Table 6 and Fig. 13 show that predicted deformations using group 2 basis functions have an excellent correlation with simulated target deformations. It should be noted that the predicted deformation on the right-hand side of the wing-tip location, at sensor number 26, is still acceptable with the group 2 basis functions, at 8.74%, even without any strain gauges on the right-hand side of the wing. The relatively large percentage difference in using the group 3 basis functions (19.6% in Table 6) is mainly caused by the inaccuracy of using the mode shapes for the basis functions, as shown in Table 6 (14.2%). The prediction difference at the left-hand side of the wing tip (4.25%) is much smaller than the prediction difference at the right-hand side of the wing tip.

Structural deformations of the X-59 QueSST aircraft are computed using measured strain data from the proof test. Therefore, the strain input $\{\epsilon_s\}$ in Eq. (5) is measured. It should be noted that the strain-gauge locations in this study are selected to verify the load equation for the future flight test, and not for structural shape sensing. Figure 14 compares predicted and measured structural deformations. In general, the group 2 basis functions give the best correlation with the target values. Large shape-sensing differences are mainly observed on structural components without strain gauges, such as the right wing, canards, and T tails. These large differences are caused by the extrapolation of the least-squares surface fitting procedure. It should be noted that the group 2 basis functions produce reasonable results at sensor numbers 25 and 26 on the right-hand side of the wing tip, as shown in Fig. 14. Basis functions based on mode shapes give an unusable deformation prediction with 83.7 and 149% errors. The maximum prediction difference with the group 2 basis functions is at the right canard position: −0.828 in. at sensor number 11. Strain gauges are not installed on the canard surfaces, as shown in Fig. 12.

IV. Conclusions

A basis function method for linear and geometrically nonlinear structural shape sensing is proposed in this study. Basis functions can be mode shapes, linear static deformation shapes, or geometrically nonlinear static deformation shapes. The proposed basis function method is validated using a high-aspect-ratio wing. The prediction difference using the nonlinear basis functions is less than 0.3% at the wing-tip section.

The swept test plate with a stress concentration is also selected as a sample case. Integration-based shape-sensing techniques are affected by the presence of a stress concentration. The basis function method gives excellent deformation prediction, even with stress concentration.

Performance of the basis functions using mode shapes and static deformation is compared using the sample case from the stabilator of the National Aeronautics and Space Administration X-59 Quiet Supersonic Technology aircraft. In most of the sample load cases, excepting load case 1, the static deformations give better prediction performance than do the mode shapes. In load case 1, the prediction error using the group 1 basis functions is smaller than the results obtained using the group 2 and group 3 basis functions at the same sensor location. When the prediction errors at all the string potentiometer locations are compared, however, the group 1

[‡]Data available online at https://www.nasa.gov/aeroresearch/nasa-x-59-calls-on-texas-for-key-testing [retrieved 24 March 2022].

Table 5 Participation factors of each basis function[a]

Basis function no.	Load case 1 Group 1	Load case 1 Group 2	Load case 1 Group 3	Load case 2 Group 1	Load case 2 Group 2	Load case 2 Group 3	Load case 3 Group 1	Load case 3 Group 2	Load case 3 Group 3	Load case 4 Group 1	Load case 4 Group 2	Load case 4 Group 3	Load case 5 Group 1	Load case 5 Group 2	Load case 5 Group 3	Load case 6 Group 1	Load case 6 Group 2	Load case 6 Group 3	Load case 7 Group 1	Load case 7 Group 2	Load case 7 Group 3
1	0.0	0.0	0.0	0.0	0.0	0.0	0.0	−0.3	0.7	0.0	−0.2	0.3	0.0	−0.1	0.1	0.0	0.2	−0.3	0.0	0.2	−0.3
2	0.0	−0.3	−0.2	0.0	0.0	0.0	0.0	−0.2	0.3	0.0	−1.2	−0.6	0.0	−0.5	−0.8	0.0	0.4	0.7	0.0	0.4	0.7
3	0.0	−2.4	1.0	0.0	−0.1	0.0	0.0	0.0	0.0	0.0	−0.7	−0.3	0.0	−0.4	−0.2	0.0	0.6	0.5	0.0	0.6	0.5
4	0.0	−1.5	2.0	0.0	−0.6	−0.5	0.0	−0.6	−1.5	0.0	0.0	0.0	0.0	−0.4	−0.7	0.0	0.5	1.1	0.0	0.5	1.1
5	0.0	−1.6	1.0	0.0	−0.8	−0.7	0.0	−1.2	−1.0	0.0	−1.5	−0.8	0.0	0.0	0.0	0.0	1.1	1.1	0.0	1.1	1.2
6	0.0	3.0	−1.4	0.0	0.5	0.3	0.0	1.4	1.4	0.0	1.3	0.7	0.0	0.8	0.6	0.0	0.0	0.0	0.0	−1.0	−1.0
7	0.0	3.0	−1.4	0.0	0.5	0.3	0.0	1.4	1.4	0.0	1.3	0.7	0.0	0.8	0.6	0.0	−1.0	−1.0	0.0	0.0	0.0
8 (mode 1R)	0.2	0.0	1.6	0.8	0.0	0.1	2.8	0.0	−1.3	−0.7	0.0	−0.5	0.8	0.0	−0.2	0.0	0.0	0.6	2.5	0.0	0.6
9 (mode 1L)	0.2	0.0	1.6	0.8	0.0	0.1	2.8	0.0	−1.3	−0.7	0.0	−0.5	0.8	0.0	−0.2	2.5	0.0	0.6	0.0	0.0	0.5
10 (mode 2R)	−0.7	0.0	0.2	0.5	0.0	0.0	1.1	0.0	−0.1	−0.7	0.0	−0.1	−0.1	0.0	−0.1	0.0	0.0	0.1	0.3	0.0	0.1
11 (mode 2L)	−0.7	0.0	0.3	0.6	0.0	0.0	1.1	0.0	−0.1	−0.7	0.0	−0.1	−0.1	0.0	−0.1	0.3	0.0	0.1	0.0	0.0	0.1
12 (mode 3R)	0.0	0.0	0.0	0.0	0.0	0.0	0.0	0.0	0.0	0.0	0.0	0.0	0.0	0.0	0.0	0.0	0.0	0.0	0.0	0.0	0.0
13 (mode 3L)	0.0	0.0	0.0	0.0	0.0	0.0	0.0	0.0	0.0	0.0	0.0	0.0	0.0	0.0	0.0	0.0	0.0	0.0	0.0	0.0	0.0
14 (mode 4R)	0.1	0.0	−0.1	−0.1	0.0	0.0	0.0	0.0	0.1	0.1	0.0	0.0	0.1	0.0	0.0	0.0	0.0	0.0	0.1	0.0	0.0
15 (mode 4L)	0.1	0.0	−0.1	−0.1	0.0	0.0	0.0	0.0	0.1	0.1	0.0	0.0	0.1	0.0	0.0	0.1	0.0	0.0	0.0	0.0	0.0
16 (mode 5R)	0.3	0.0	0.2	−0.1	0.0	0.0	−0.1	0.0	−0.2	0.1	0.0	−0.1	0.1	0.0	0.0	0.0	0.0	0.1	0.1	0.0	0.1
17 (mode 5L)	0.3	0.0	0.2	−0.1	0.0	0.0	−0.1	0.0	−0.2	0.1	0.0	−0.1	0.1	0.0	0.0	0.1	0.0	0.1	0.0	0.0	0.1

[a]R denotes right stabilator, and L denotes left stabilator.

Fig. 11 Proof test of the X-59 Quiet Supersonic Technology aircraft. Credits: Lockheed Martin Corporation.

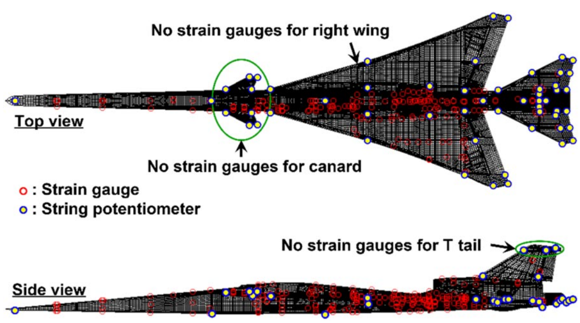

Fig. 12 Locations of strain gauges and string potentiometers on the X-59 Quiet Supersonic Technology aircraft.

basis functions give the worst performance. Mainly, the mode shapes of the low-frequency modes participate in structural shape sensing.

Wing shape sensing with sparse strain data is also demonstrated in this study using the X-59 QueSST aircraft. Strain gauges are not installed on the right wing, canards, t tails, flaps, or ailerons. The maximum prediction errors using the group 1 and group 3 basis functions at sensor identification number 26 location (the right wing-tip section) are 3.769 in. (83.7% error) and 6.731 in. (149% error), respectively. On the other hand, the maximum prediction error using the group 2 basis function is 0.557 in. (12.4% error) at the same string potentiometer location. The predicted deformations have a good match with the target deformations.

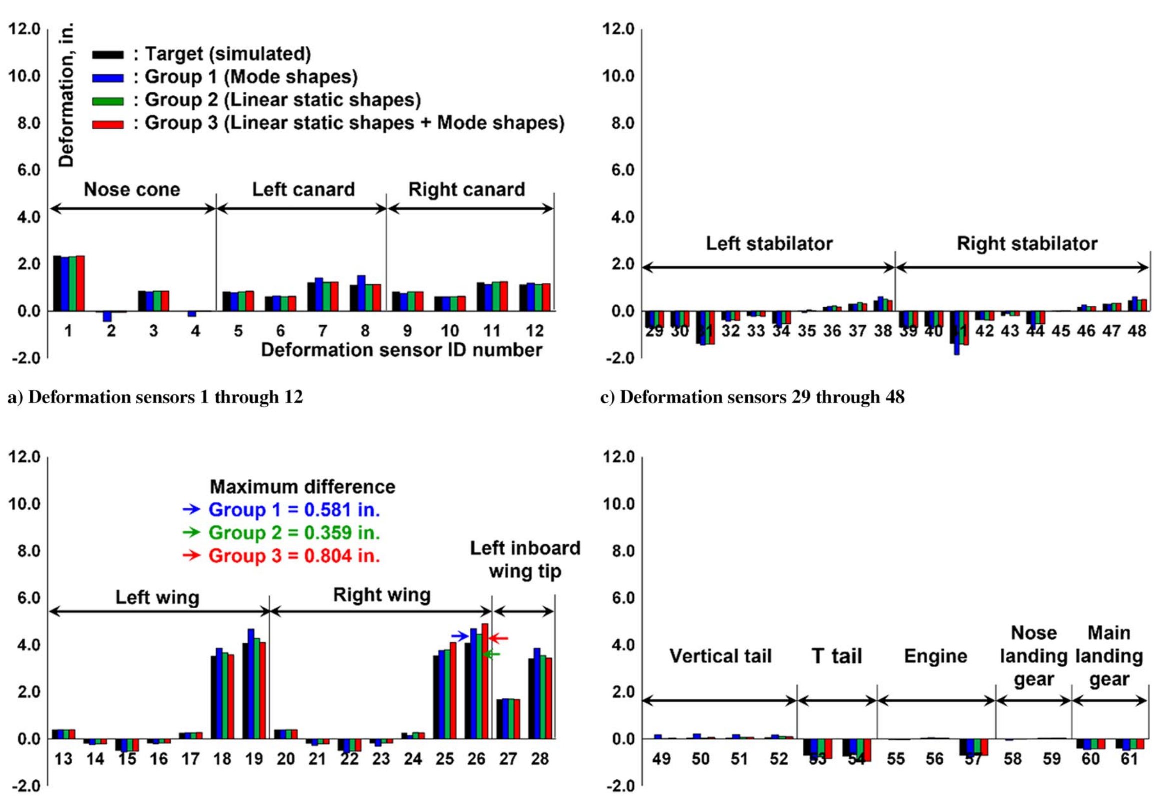

a) Deformation sensors 1 through 12

c) Deformation sensors 29 through 48

b) Deformation sensors 13 through 28

d) Deformation sensors 49 through 61

Fig. 13 Comparisons of simulated vertical deformations under different basis function groups for load case 2.

Table 6 Comparisons of Z deformation using different basis functions for load case 2[b]

Target deformation, in.	Maximum target deformation, in. (PID #)	Deformation at mirror image location of maximum target deformation, in. (PID #)	Group 1 (mode shapes: 30) Difference, in. (%)[a]	Group 1 (mode shapes: 30) Maximum difference, in. (pot. ID #)	Group 2 (static shapes: 24) Difference, in. (%)[a]	Group 2 (static shapes: 24) Maximum difference, in. (PID #)	Group 3 (group 1 + group 2) Difference, in. (%)[a]	Group 3 (group 1 + group 2) Maximum difference, in. (PID #)
Simulated	4.104 (26)		0.581 (14.2)	0.581 (26)	0.359 (8.74)	0.359 (26)	0.804 (19.6)	0.804 (26)
		4.099 (19)	0.578 (14.1)		0.174 (4.25)		0.004 (0.10)	
Measured		4.501 (26)	3.769 (83.7)	3.769 (26)	−0.557 (−12.37)	−0.828 (11)	6.731 (149.)	6.731 (26)
	4.554 (19)		−0.050 (−1.09)		−0.411 (−9.02)		−0.278 (−6.11)	

[a]Difference between target deformation and predicted deformation

[b]PID 19 denotes the left wing tip, where the strain gauges are located; PID 26 denotes the right wing tip, where strain gauges are not located; and PID 11 denotes the right forward outboard canard, where strain gauges are not located.

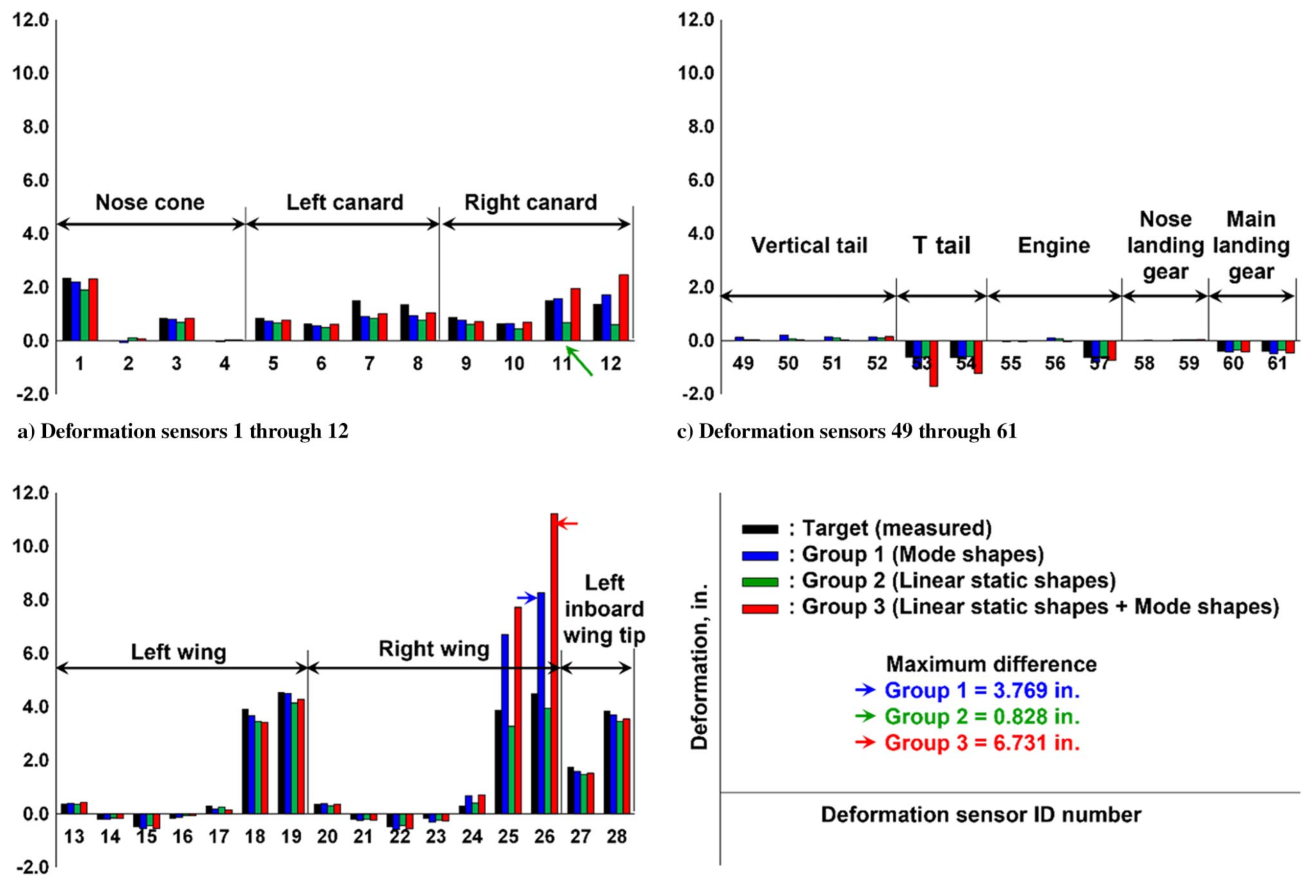

a) Deformation sensors 1 through 12

c) Deformation sensors 49 through 61

b) Deformation sensors 13 through 28

Fig. 14 Comparisons of measured vertical deformations under different basis function groups for load case 2.

Appendix A: Computation of the Nodal Weighting Factors

A coordinate transformation for quadrilateral shapes from the 3-D global space to the two-dimensional (2-D) local plane is summarized in Fig. A1. First, as shown in Fig. A1b, the four corner nodes in Fig. A1a are transformed into 2-D planes. To ensure the uniqueness of the transformation, the first corner node (x_1, y_1, z_1) and second corner node (x_2, y_2, z_2) are located at the origin and on the X axis, respectively, as shown in Fig. A1b. The coordinate transformation from the quadrilateral shape in Fig. A1b to the square parent shape in Fig. A1c is performed using the isoparametric shape functions [19] as shown in Eqs. (A1–A3):

$$X = \sum_{i=1}^{4} N_i(\xi, \eta)\{X_i\} \tag{A1}$$

$$Y = \sum_{i=1}^{4} N_i(\xi, \eta)\{Y_i\} \tag{A2}$$

$$\begin{aligned} N_1(\xi,\eta) &= \frac{(1+\xi)(1+\eta)}{4} \\ N_2(\xi,\eta) &= \frac{(1-\xi)(1+\eta)}{4} \\ N_3(\xi,\eta) &= \frac{(1-\xi)(1-\eta)}{4} \\ N_4(\xi,\eta) &= \frac{(1+\xi)(1-\eta)}{4} \end{aligned} \tag{A3}$$

Substituting Eq. (A3) into Eqs. (A1) and (A2) gives Eqs. (A4) and (A5):

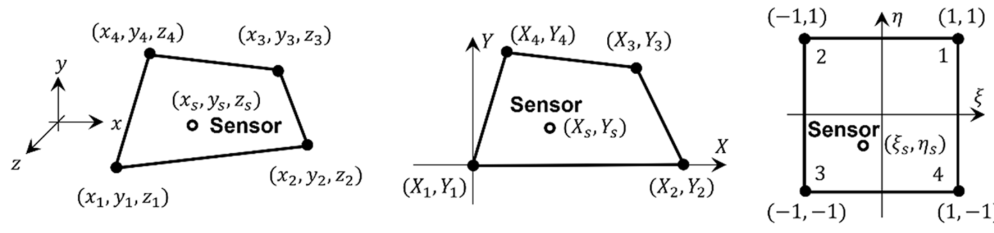

a) Quadrilateral shape in 3-D space b) Quadrilateral shape in 2-D plane c) Square shape in 2-D parent element

Fig. A1 Coordinate transformation for quadrilateral shapes.

$$4X = a + b\xi + c\eta + d\xi\eta \tag{A4}$$

$$4Y = e + f\xi + g\eta + h\xi\eta \tag{A5}$$

where Eq. (A6) is

$$\begin{aligned}
a &= X_1 + X_2 + X_3 + X_4 \\
b &= X_1 - X_2 - X_3 + X_4 \\
c &= X_1 + X_2 - X_3 - X_4 \\
d &= X_1 - X_2 + X_3 - X_4 \\
e &= Y_1 + Y_2 + Y_3 + Y_4 \\
f &= Y_1 - Y_2 - Y_3 + Y_4 \\
g &= Y_1 + Y_2 - Y_3 - Y_4 \\
h &= Y_1 - Y_2 + Y_3 - Y_4
\end{aligned} \tag{A6}$$

The sensor coordinates in the parent element in Fig. A1c are calculated using Eqs. (A4–A6), as well as the coordinates in Fig. A1b. Substituting (ξ_s, η_s) values into Eq. (A3) gives the nodal weighting factors for quadrilateral shapes.

The nodal weighting factors for the triangular shapes in Fig. A2a are calculated using an area coordinate in Eq. (A7). Similarly, the nodal weighting factors in Eq. (A8) are used for line shapes in Fig. A2b:

$$\begin{aligned}
N_1 &= \frac{A_1}{A_1 + A_2 + A_3} \\
N_2 &= \frac{A_2}{A_1 + A_2 + A_3} \\
N_3 &= \frac{A_3}{A_1 + A_2 + A_3}
\end{aligned} \tag{A7}$$

$$\begin{aligned}
N_1 &= \frac{L_1}{L_1 + L_2} \\
N_2 &= \frac{L_2}{L_1 + L_2}
\end{aligned} \tag{A8}$$

Appendix B: Geometrically Nonlinear Two-Step Theory

A block diagram of the mathematical background of the two-step theory [10] is shown in Fig. B1. All three blocks are about the first step: except the upper-right block, which is the second step. The first step of the nonlinear two-step theory can be summarized as follows:

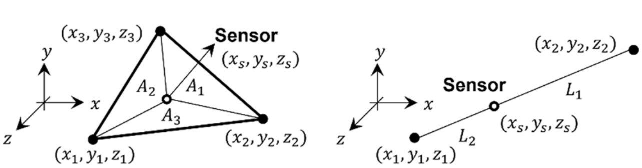

a) Triangular shape in 3-D space b) Line shape in 3-D space

Fig. A2 Area and length coordinates for triangular and line shapes.

1) Take axial strain measurements along each fiber-optic strain sensing line. A strain on one side and corresponding strain on the other side of the structure are needed to compute the curvature.

2) Compute the curvature along each FOSS line. Multiple straight bar elements should be defined along the FOSS line. The centroids of the elements should match the strain measuring points. Assume that each element is under constant strain. In each bar element, compute the curvature defined in Eq. (B1):

$$\kappa = -\frac{\epsilon_u - \epsilon_l}{h} = \frac{d^2 w(\tilde{s})}{d\tilde{s}^2} \tag{B1}$$

3) Compute the slope and deformation along each fiber line. Integrate Eq. (B1); then, the slope is available as in Eq. (B2):

$$\frac{dw(\tilde{s})}{d\tilde{s}} \tag{B2}$$

When Eq. (B2) is integrated, the linear deformation in the fiber direction $w(\tilde{s})$, shown in Fig. B2a, is obtained. Therefore, geometrically nonlinear deformation ($\Delta\tilde{s}$ and $\Delta\tilde{z}$ in "fiber coordinates") can be computed.

4) A local dihedral, anhedral, or taper effect (angle α in Fig. B2b) should be included in the deformation computation. Rotate the deformations $\Delta\tilde{s}$ and $\Delta\tilde{z}$ to have Δs and Δz in Fig. B2b.

5) Finally, in Fig. B2c, include the curved fiber effect (angle β). Calculate the deformations Δx and Δy from Δs.

In the second step, computed deformations from the first step are expanded to the entire structure using the system equivalent reduction and expansion process (SEREP) [20]. Rearrange all the degrees of freedom (DOFs) in the FE model as in Eq. (B3):

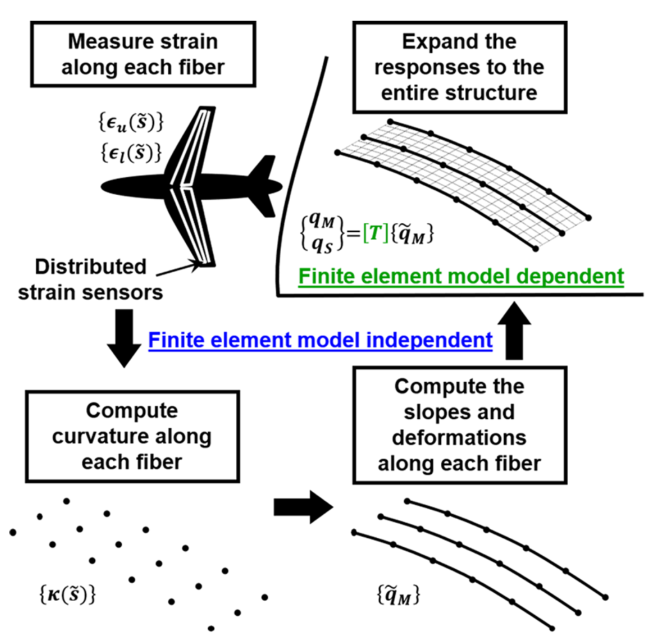

Fig. B1 Block diagram of the two-step theory.

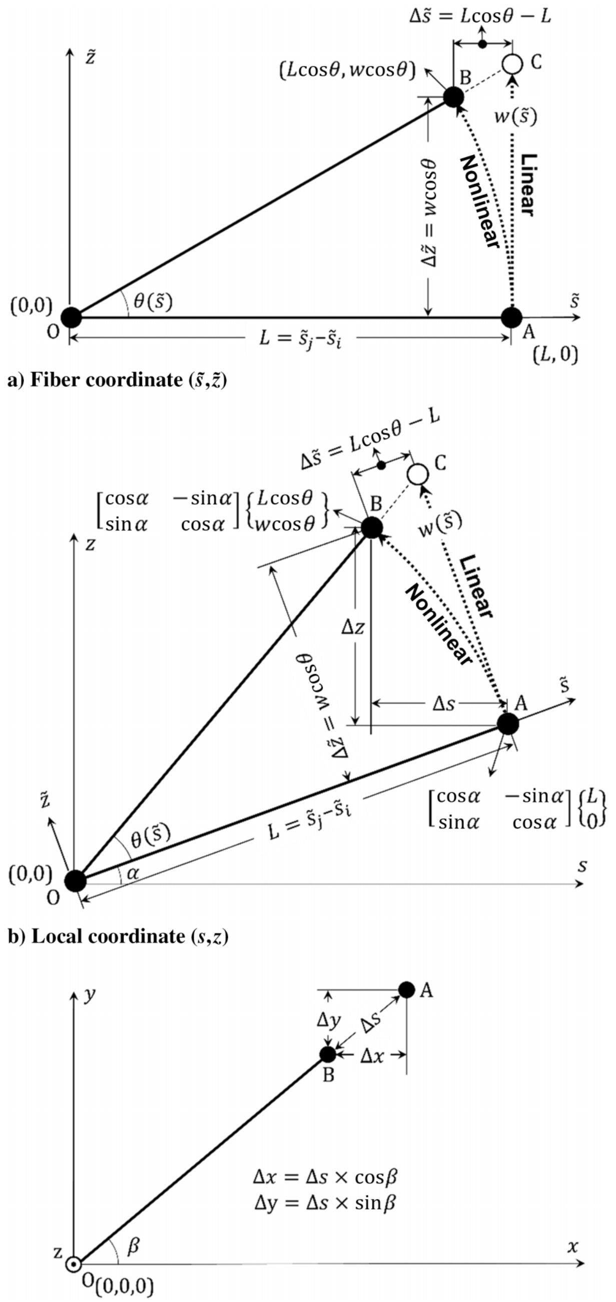

a) Fiber coordinate ($\tilde{s}$,$\tilde{z}$)

b) Local coordinate (s,z)

c) Global coordinate (x,y,z)

Fig. B2 Representations of a) fiber; b) local; and c) global coordinate system for deformation computations.

$$\{q\} = \begin{Bmatrix} q_M \\ q_S \end{Bmatrix} \tag{B3}$$

where $\{q_M\}$ is the master DOF. In this approach, deformations from the first step are defined as the master DOFs. The rest of the deformations all over the structure are defined as slave DOFs $\{q_S\}$. Consider the following coordinate transformation for the model reduction and expansion techniques as in Eq. (B4):

$$\begin{Bmatrix} q_M \\ q_S \end{Bmatrix} = [\boldsymbol{T}]\{\tilde{q}_M\} \tag{B4}$$

where $\{\tilde{q}_M\}$ is the measured master DOF, which was computed from the first step. From the SEREP, the transformation matrix [T] can be expressed as Eq. (B5):

$$[\boldsymbol{T}] = \begin{bmatrix} \boldsymbol{\Phi}_M(\boldsymbol{\Phi}_M^T\boldsymbol{\Phi}_M)^{-1} & \boldsymbol{\Phi}_M^T \\ \boldsymbol{\Phi}_S(\boldsymbol{\Phi}_M^T\boldsymbol{\Phi}_M)^{-1} & \boldsymbol{\Phi}_M^T \end{bmatrix} \tag{B5}$$

where $\boldsymbol{\Phi}_M$ and $\boldsymbol{\Phi}_S$ are basis functions corresponding to master and slave DOFs, respectively. These basis functions are mode shapes and/or static deformation shapes. From Eqs. (B3–B5), all the DOFs in the structure can be computed using Eq. (B6):

$$\{q\} = \begin{Bmatrix} q_M \\ q_S \end{Bmatrix} = \begin{bmatrix} \boldsymbol{\Phi}_M(\boldsymbol{\Phi}_M^T\boldsymbol{\Phi}_M)^{-1} & \boldsymbol{\Phi}_M^T \\ \boldsymbol{\Phi}_S(\boldsymbol{\Phi}_M^T\boldsymbol{\Phi}_M)^{-1} & \boldsymbol{\Phi}_M^T \end{bmatrix}\{\tilde{q}_M\} \tag{B6}$$

Acknowledgments

The work presented in this paper was funded by the Low-Boom Flight Demonstration Project under the NASA Aeronautics Research Mission Directorate. The author thanks peer review committee members Benjamin Park, Samson Truong, and Ashante Jordan of the NASA Neil A. Armstrong Flight Research Center.

References

[1] Noll, T. E., Brown, J. M., Perez-Davis, M. E., Ishamael, S. D., Tiffany, G. C., and Gaier, M., "Investigation of the Helios Prototype Aircraft Mishap," Vol. 1, NASA Mishap Report, 2004, https://www.nasa.gov/pdf/64317main_helios.pdf [retrieved 12 Oct. 2018].

[2] Pak, C.-G., "Jig-Shape Optimization of Low-Boom Supersonic Aircraft," *Journal of Aircraft*, Vol. 55, No. 5, 2018, pp. 2154–2161. https://doi.org/10.2514/1.c034851

[3] Foss, G. C., and Haugse, E. D., "Using Modal Test Results to Develop Strain to Displacement Transformation," *Proceedings of the 13th International Modal Analysis Conference*, Soc. for Experimental Mechanics, Inc., Feb. 1995, pp. 112–118.

[4] Kang, L., Kim, D., and Han, J., "Estimation of Dynamic Structural Displacements Using Fiber Bragg Grating Strain Sensors," *Journal of Sound and Vibration*, Vol. 305, No. 3, 2007, pp. 534–542. https://doi.org/10.1016/j.jsv.2007.04.037

[5] Freydin, M., Rattner, M. K., Raveh, D. E., Kressel, I., Davidi, R., and Tur, M., "Fiber-Optics-Based Aeroelastic Shape Sensing," *AIAA Journal*, Vol. 57, No. 12, Dec. 2019, pp. 5094–5103. https://doi.org/10.2514/1.J057944

[6] Tessler, A., and Spangler, J. A., "Variational Principle for Reconstruction of Elastic Deformations in Shear Deformable Plates and Shells," NASA TM-212445, 2003.

[7] Ko, W. L., Richards, W. L., and Tran, V. T., "Displacement Theories for In-Flight Deformed Shape Predictions of Aerospace Structures," NASA TP-2007-214612, 2007.

[8] Bakalyar, J., and Jutte, C., "Validation Tests of Fiber Optic Strain-Based Operational Shape and Load Measurements," AIAA Paper 2012-2904, 2012. https://doi.org/10.2514/6.2012-1904

[9] Derkevorkian, A., Masri, S. F., Alvarenga, J., Boussalis, H., Bakalyar, J., and Richards, W. L., "Strain-Based Deformation Shape-Estimation Algorithm for Control and Monitoring Applications," *AIAA Journal*, Vol. 51, No. 9, Sept. 2013, pp. 2231–2240. https://doi.org/10.2514/1.J052215

[10] Pak, C.-G., "Wing Shape Sensing from Measured Strain," *AIAA Journal*, Vol. 54, No. 3, 2016, pp. 1068–1077. https://doi.org/10.2514/6.2015-1427

[11] Pak, C.-G., and Truax, R. A., "Acceleration and Velocity Sensing from Measured Strain," AIAA Paper 2016-1229, 2016. https://doi.org/10.2514/6.2016-1229

[12] Pak, C.-G., "Unsteady Aerodynamic Force Sensing from Strain Data," *Journal of Aircraft*, Vol. 54, No. 4, 2017, pp. 1476–1485. https://doi.org/10.2514/1.c034140

[13] Pak, C.-G., "Shape Sensing for Wings with Spars and Ribs Using Simulated Strain," *AIAA SciTech Conference*, AIAA Paper 2019-1756, Jan. 2019. https://doi.org/10.2514/6.2019-1756

[14] Su, W., and Cesnik, C. E. S., "Nonlinear Aeroelasticity of a Very Flexible Blended-Wing-Body Aircraft," *AIAA Journal*, Vol. 47, No. 5, 2010, pp. 1539–1553. https://doi.org/10.2514/1.47317

[15] Ko, W. L., Tran, V. T., and Lung, S.-F., “Curved Displacement Transfer Functions for Geometric Nonlinear Large Deformation Structure Shape Predictions,” NASA TP-2017-219406, 2017.

[16] Drachinsky, A., and Raveh, D. E., “Modal Rotations: A Modal-Based Method for Large Structural Deformations of Slender Bodies,” *AIAA Journal*, Vol. 58, No. 7, 2020, pp. 3159–3173.
https://doi.org/10.2514/1.J058899

[17] Suh, P. M., Chin, A., and Mavris, D. N., “Robust Modal Filtering and Control of the X-56A Model with Simulated Fiber Optic Sensor Failures,” *AIAA Atmospheric Flight Mechanics Conference*, AIAA Paper 2014-2053, June 2014.
https://doi.org/10.2514/6.2014-2053

[18] *MSC Nastran 2018 Quick Reference Guide*, MacNeal-Schwendler, Newport Beach, CA, 2017.

[19] Zienkiewicz, O. C., *The Finite Element Method*, 3rd ed., McGraw–Hill, New York, 1977.

[20] O’Callahan, J., Avitabile, P., and Riemer, R., “System Equivalent Reduction Expansion Process,” *Proceedings of the 7th International Modal Analysis Conference*, Las Vegas, NV, 1989, pp. 29–37.

S. Shin
Associate Editor